Radiation in Art and Archeometry

Edited by

D.C. Creagh

Faculty of Information Science and Engineering
Division of Management and Technology
University of Canberra
Canberra
Australia

and

D.A. Bradley

School of Physics
University of Exeter
Exeter
United Kingdom

First edition 2000

Synchrotron Radiation Tomographic Energy-Dispersive Diffraction Imaging

S. L. Colston, A. C. Jupe and P. Barnes

Industrial Materials Group, Crystallography Department, Birkbeck College, Malet St., London WC1E 7HX, United Kingdom

A description of the synchrotron energy-dispersive x-ray powder diffraction method and its particular advantages is given first. Example applications are illustrated with data collected from various samples, including archaeological objects.

1. INTRODUCTION

The ability of x-rays to 'see into' solid objects was their first observed property, and of course it is still the most widely known. X-ray photographs give excellent spatial resolution, but they only show changes in absorbance, and give no explicit information about sample composition. Our aim in developing x-ray diffraction tomography is to combine spatial resolution with the crystalline phase information available from diffraction data. For several reasons, conventional laboratory x-ray sources are not suitable for this technique, and we must turn to synchrotron sources instead.

The world's first dedicated synchrotron radiation source was built at Daresbury, UK and became operational in the early 1980's, and today such facilities are to be found in every continent. Synchrotrons have several significant advantages over traditional laboratory x-ray sources. These are in essence, that the beam contains a continuous spectrum of wavelengths, is highly collimated, and is many orders of magnitude more intense than that obtained from a sealed tube source. The impact of synchrotron radiation on the application of the powder diffraction method has been immense in many respects. An excellent example of this is the energy-dispersive diffraction (EDD) method, which has emerged as a powerful tool for time resolved studies of chemical reactions such as zeolite synthesis and cement hydration. More recently, we have been exploiting the rapidity and unconventional geometry of EDD, developing a spatially resolved diffraction technique, which we refer to somewhat loosely as tomographic energy-dispersive diffraction imaging, or TEDDI. TEDDI has several features of particular interest for the characterisation of archaeological objects.

1. It can probe a selected small volume element or series of volume elements within a sample, *i.e:* it can give spatially resolved information. The sample volume element for each diffraction pattern is selected by positioning the sample appropriately in the x-ray beam.
2. The radiation is intense and penetrating, so even relatively bulky samples can be analysed.
3. It is a non-destructive method (provided that beam damage does not occur) and it requires no special sample preparation.
4. As a powder diffraction method, it is essentially equivalent to conventional laboratory diffractometry in that it gives data from which we can make reliable mineral phase identifications.

5. Data sets can be acquired rapidly (within seconds or minutes depending on the sample) so a relatively large number of volume elements can be probed in a reasonable time.

'Small volume element' here means typically a needle-shaped region about 0.5 mm in cross-section and a few millimetres in length. These dimensions vary from one experiment to another, but in general we can easily obtain good enough spatial resolution to distinguish, for instance, weathering products in the outer layers of a piece of masonry, or crystalline kiln firing products in a ceramic artefact. As far as we can tell, most mineral samples are neither chemically nor mechanically affected by exposure to the beam, but certain materials (*e.g.* glasses, and halides such as common salt) may undergo objectionable discoloration. This effect can be minimized or eliminated where it occurs by using short data collection times, or by attenuating the damaging low-energy radiation by placing a sheet of aluminium in the incident beam.

1.1 Theory of EDD

EDD was first demonstrated by Geissen and Gordon [1]. It is perhaps most readily understood by comparison with the angle-dispersive Debye-Scherrer camera method, in which a powder sample in a glass capillary is encircled by a radiation sensitive film. The sample is irradiated with a monochromatic (single-wavelength) beam, and scattered x-rays are registered by the film at all angles ,2θ, in the plane normal to the capillary axis. The EDD set-up may be seen as the inverse of this, in that the sample is irradiated with a 'white' beam (containing a continuous range of wavelengths), the scattered radiation being measured at only a single angle. The EDD experimental setup is distinctive in two respects.

1. The speed of data collection is not limited by moving parts within the apparatus.
2. The diffraction pattern is not acquired systematically as in a conventional diffractometer, but is allowed to accumulate for some chosen period of time.

A schematic representation of an EDD diffractometer is given in Figure 1. The diagram is by no means drawn to scale! The important points are:

1. the beam passes completely through the sample, which is placed between source and detector;
2. only x-ray photons scattered through a chosen angle are allowed to enter the detector. This angle (2θ) is selected by the collimator. Typically the spacing between the molybdenum collimator plates is 0.1 mm or less, and the distance from sample to collimator is 200–500 mm, so that 2θ is quite sharply defined. This is important if we are to obtain reasonably well-resolved diffraction peaks, since the greater the collimator plate separation, the broader the peaks will become, especially at the low 2θ settings (about 2–8°) which are commonly used.
3. Only a defined portion of the sample contributes to the diffraction pattern. This is the volume contained by the intersection of the incident beam with the 'line of sight' of the collimator. If the sample is translated (since we cannot move the synchrotron) a different part of it will be 'seen' in the diffraction data. This is the principle of spatially resolved TEDDI.

Clearly, EDD data collection requires a detector that not only measures the diffracted beam intensity, but also its wavelength spectrum. A detector that not only counts photons but also measures their energies will serve, since we can convert between photon energy
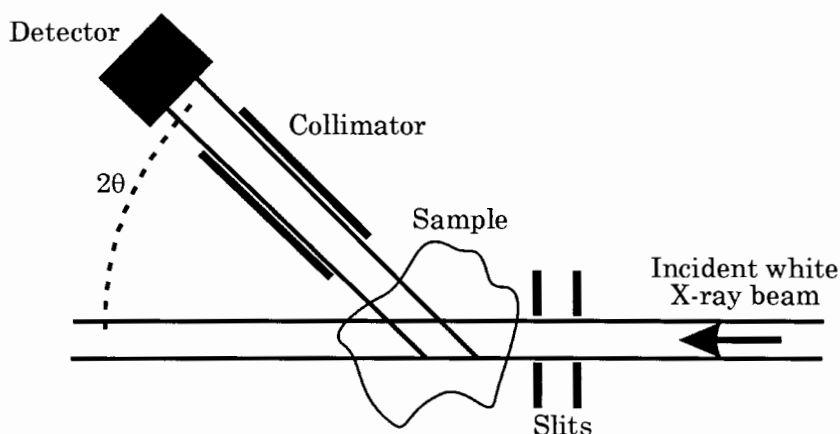
Figure 1. Schematic diagram of an energy-dispersive diffractometer. The intersection of the incident and diffracted beams defines the diffracting volume or 'needle'.

distribution and wavelength spectrum using the Planck-Einstein photon energy relation $E=hc/\lambda$ where h and c are Planck's constant and the speed of light respectively. The authors of [1] used a lithium-doped Si crystal detector of the type used for fluorescence microprobe analysis in scanning electron microscopy, but the intrinsic Ge crystal detector is now universally preferred for its greater efficiency in detecting the higher energy photons which are of interest for EDD. As an example, the range of detection for the EDD instrument at the Daresbury SRS is chosen to be about 6–113 keV. Owing to the ≈6 keV lower limit, fluorescence lines from elements below Fe in the periodic table are excluded from the data. Note, however, that this is of little practical importance, since generally we are only interested in Bragg reflections and the information they give us about which crystalline phases are present in the sample.

How do we use diffraction data to identify crystalline phases? A complete and coherent exposition of the theory of x-ray diffraction by crystals would require a whole chapter in itself. Such chapters are to be found in all of the many textbooks on x-ray crystallography, but it is appropriate to give at least a very brief outline of the principles involved, in order to highlight the equivalence between EDD and convention angle-scanning diffraction (ASD).

A crystal consists, by definition, of an orderly array of building blocks known as unit cells, each unit cell containing an identical arrangement of atoms. Thus a well-crystallised material such as quartz can be described as a periodic array of atoms: this is why crystals are able to diffract x-rays. The crucial point is that in practice, the size and shape of the unit cells, and thus the periodicity of the crystal, are unique to any one crystalline compound. X-ray diffraction enables us to quantify the periodicity (the separation or d spacing of crystal planes) from which we are able to identify each phase present in the sample. In other words, every crystalline material has its own 'signature' in a diffraction pattern.

The periodicity actually extends to more than three directions. For any crystal, there are numerous, though prescribed, directions along which the arrangement of atoms repeats itself regularly. The periodicity in each of these directions can be characterised by a d spacing corresponding to that direction, and each peak in a diffraction pattern corresponds to a d spacing characteristic of some component of the sample, the positions of the peaks being determined by the d spacings. The x-ray diffraction patterns of tens of thousands of inorganic phases have been measured, and collected into a database by the International Centre for

Diffraction Data (ICDD). Each entry lists peaks according to their corresponding d-spacings and relative intensities. Regardless of which experimental set-up we choose for data collection, if we can assign a d spacing to each peak in the diffraction pattern obtained, we should be able to use the database to help interpret what we see.

With conventional angle-dispersive diffraction, the traditional Bragg equation

$$\lambda = 2d\sin\theta \tag{1}$$

is used to convert a scattering angle 2θ to a d spacing, since the fixed radiation wavelength λ is known in advance. This can be recast into a more convenient form for EDD with the help of the photon energy relation $E=hc/\lambda$. Combining this with equation (1) (and using appropriate units for the physical constants h and c) we get

$$Ed\sin\theta = 6.19926 \text{ keV·Å} \tag{2}$$

This gives us a simple relationship between d and the photon energy E at which Bragg reflection takes place, since owing to the fixed detector angle, sin• is now constant.

Figure 2 shows two datasets collected in 5 minutes from a sample of gypsum, (thickness 8 mm), with a 0.5×0.5 mm incident beam. For the data shown in Figure 2(a), the detector angle was set to 5.1°. Substituting this value into equation (2) and rearranging a little gives

$$d = 6.19926/(E\sin\theta) = 6.19926/(E\times\sin(5.1/2)) = 6.19926/(E\times\sin(2.55))$$
$$= 139.34/E \tag{3}$$

For this reason, the plots in Figure 2 have dual x axes, with an energy scale below and a $10/d$ scale above.

Table 1 shows the strongest peak positions and their corresponding d spacings. The peak intensities can be seen to be very high, and indeed the collection time could have shortened (to 1 or two minutes, say) without significant loss of data quality. Although the peaks are positioned as expected, the relative intensities differ from those in the ICDD database. The main reason for this is that the synchrotron white beam is not equally intense for all photon energies. This is why, for instance, the peak at 18.33 keV is much weaker than expected compared to the peak at 45.5 keV, where the beam is much more intense. At the Daresbury SRS we expect a similar weakening of intensities above about 70 keV. Provided that we bear these factors in mind, however, the discrepancies are not so great as to seriously impede phase identification. This is particularly true when (as usually) we have some prior knowledge of the sample composition. The effect of changing the detector angle can be seen clearly from a comparison of Figures 2(a) and 2(b).

Table 1
Details of EDD peaks from gypsum ; $2\theta = 5.1°$

Energy (keV)	Calculated d spacing	Reflection hkl	2θ for Cu K_α (ASD)
18.33	7.60	020	11.59°
32.53	4.28	021	20.72°
45.46	3.06	041	29.11°
48.50	2.87	-221	31.10°

$10/d$ (Å^{-1})
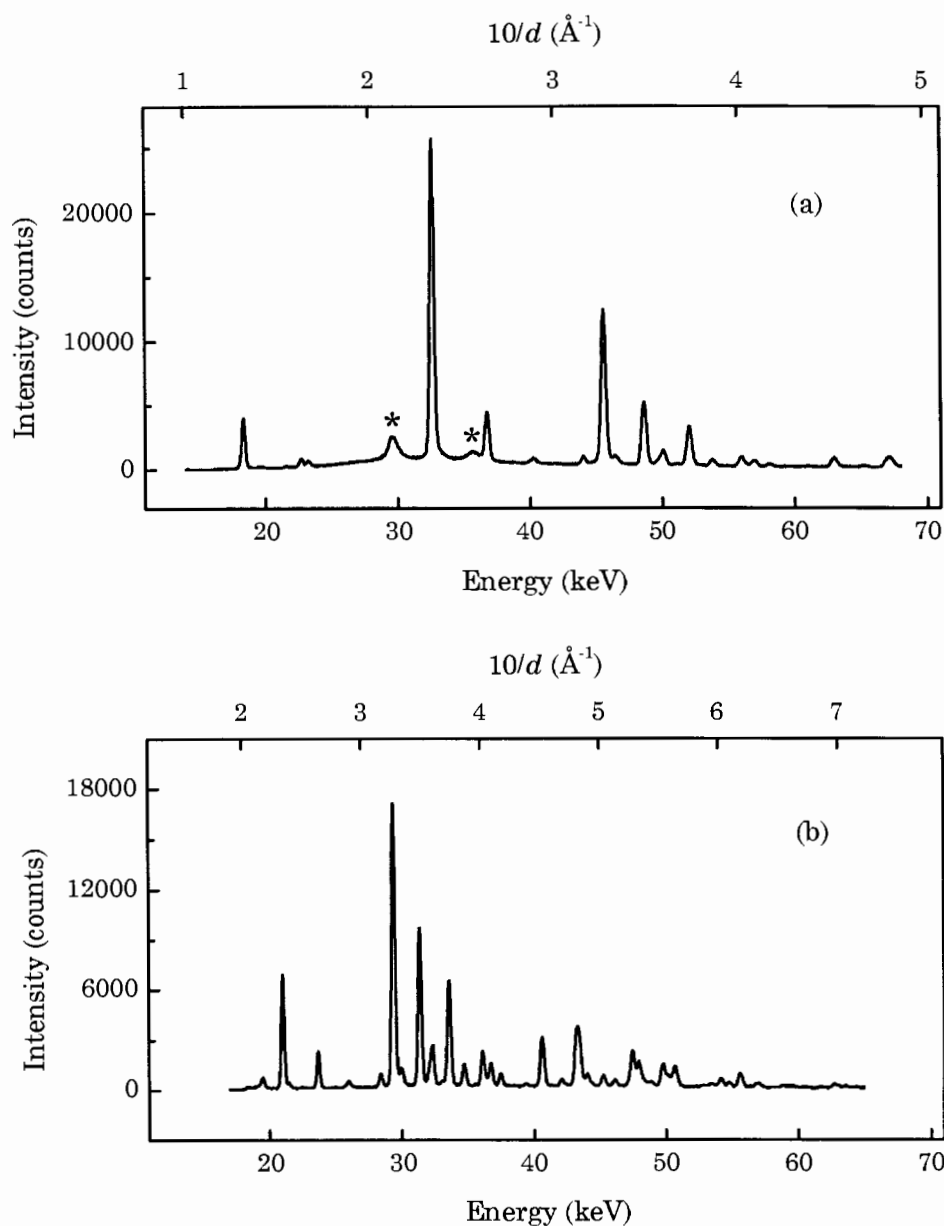

$10/d$ (Å^{-1})

Figure 2. EDD data from a sample of gypsum. 2θ settings were 5.1° in (a) and 7.9° in (b). The peaks marked (*) in (a) are due to the PEEK sample holder. The x scales show photon energy below and $10/d$ above. Note the more condensed $1/d$ scale in (b), and the correspondingly greater density of peaks with respect to the energy scale.

Figure 2(b) shows data again from a gypsum sample, but with 2θ set to 7.9°. It is immediately apparent that the density of peaks is greater at the higher angle. EDD is a relatively low-resolution diffraction technique, so ideally we would like to maximise the separation between adjacent peaks, and so avoid peak overlap. Overlaps between peaks may make weaker peaks more difficult to identify, and generally hampers the precise determination of individual peak intensities. Choosing a lower detector angle in EDD is equivalent to choosing a longer wavelength in conventional diffraction. In both cases peaks are shifted further apart and upwards in energy (EDD) or 2θ (angle-dispersive). This is not the only, or even the primary consideration, to be made when the detector angle is chosen, however, because our main aim is to capture as many strong peaks as possible from such phases as may be present in our sample. A fuller account of the theory of EDD can be found in [2], which also contains a copious list of further references.

Figure 3 [3] shows the relative intensity of the incident beam as a function of photon energy. There is a clear maximum at about 38 kV, although the reduced flux at the high-energy end of the spectrum is offset by the enhanced sample penetration of the higher energy radiation. As the useful energy range is essentially fixed, the range of d spacing coverage is determined by the detector angle; for larger d spacing, we need a lower angle. Table 2 shows the observable range for several 2θ settings, assuming a useful energy range of 30–100 keV.

What is the best range to select? Fortunately, there *is* a reasonably general answer to this question; the ICDD database shows that nearly 80% of known inorganic crystals give strongest Bragg reflections in the 5–2 Å range. Thus a detector angle of about 4.7° would seem to be a reasonable choice in general. We should, however, qualify this by pointing out that with this setting some clay and zeolite minerals with strong reflections at longer d spacings (to 10 Å or greater) may be difficult to detect. At the Daresbury SRS this limitation is surmounted by the use of an array of three detectors, collecting data simultaneously at three angles; this is not universal practice. (Note that the choice of a lower detector angle is
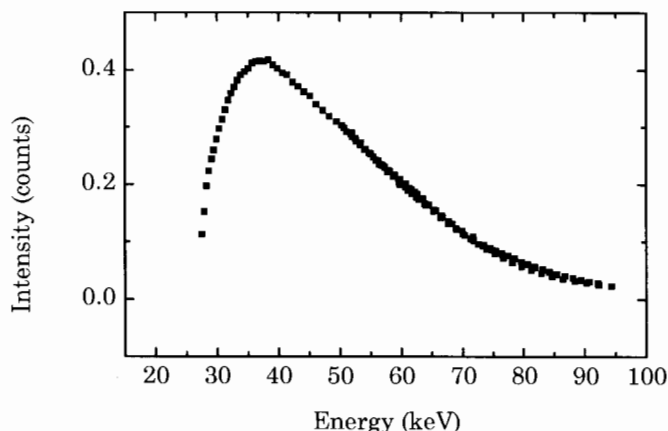

Figure 3. Relative beam flux from beamline 16 at SRS Daresbury, as a function of energy. The points are based on experimentally determined values.

Table 2
d-spacing ranges

2θ detector angle	lower d-spacing (Å) (at 30keV)	upper d-spacing (Å) (at 70keV)
2.0	4.4	17.7
5.0	1.8	7.1
8.0	1.11	4.4

equivalent to the choice of a longer x-ray in ASD. However, EDD is not a substitute for small angle-dispersive diffraction techniques as d-spacings longer than about 20 Å are difficult to measure, and the d-spacing resolution is probably not adequate for this purpose.

The detector angle crucially determines the shape of the diffracting volume within the sample. This is a very important where spatial resolution is a primary objective.

1.2 The Diffracting Needle

To get the best spatial resolution, clearly we would like the diffracting volume to be as small as possible. The synchrotron beam is very intense and has a very small angle of divergence, so we can make the incident beam cross-sectional area quite small (*i.e.,* 0.1×0.1 mm) to minimise the volume in directions transverse to the beam. Unfortunately, we have less control over the length of the diffracting volume along the beam direction. This length depends on the detector angle and the width of the diffracted beam collimator, as well as on the size of the incident beam, but with these set to useable values, the length of the diffracting volume is typically several millimetres. If we assume that both incident and diffracted beams are parallel (which is a reasonable assumption as long as the diffracted beam collimator is narrow enough) the length of the diffracting volume L is given by

$$L = W_I/\sin\theta + W_D/\tan\theta \qquad (4)$$

where W_I is the collimator plate separation, and W_D is the vertical size of the incident beam.
In the range of 2θ commonly used, $\sin\theta \approx \tan\theta \approx \theta$ (θ in radians), and to a good approximation, $L \propto 1/\theta$; as we would expect, the diffracting volume elongates along the beam axis as 2θ is

Table 3
Diffraction needle lengths

Detector 2θ	Beam size (mm)	Diffraction needle length (mm)
2	0.1	4.30
2	0.2	7.16
2	0.5	15.75
5	0.1	2.29
5	0.2	3.43
5	0.5	6.86
8	0.1	1.43
8	0.2	2.14
8	0.5	4.28

lowered. Typically, L is 5–15 mm, and the diffracting volume resembles a compass needle when viewed from the side, rather than the lozenge shape seen in Figure 1, and we refer to it as the diffraction 'needle'. Clearly, spatial resolution is much more limited in the direction parallel to the incident beam than in directions perpendicular to it. Table 2 lists calculated needle lengths for some typical 2• settings, beam sizes and collimator plate separations.

We have yet one other constraint to consider. We need to sweep out a certain (usually relatively large) volume of our sample within a limited time period, while obtaining diffraction data of adequate quality. From this point of view, reducing the diffracting volume is disadvantageous in two ways. Firstly, we need to collect more data sets, and secondly, we will need to spend more time collecting each set, because the smaller diffracting volume will result in lower diffracted intensities. In all, we can deduce that as a rule-of-thumb, the overall data collection time requirement is proportional to V/v^2 where V is the overall sample volume to be traversed, and v is the diffracting volume, for a given peak-to-noise ratio in the data. Because of this, we can sensibly argue that if spatial resolution is required in only one or two directions, the extension of the diffraction needle along the beam axis is actually an advantage. It enables more rapid data collection (provided that the needle is fully contained within the bulk of the sample object). Applications such as probing for surface weathering products can benefit from this diffraction needle geometry. For true three-dimensional imaging, we could in principle collect a second matrix of data sets after turning the sample through 90° about a vertical axis and collating all of the data appropriately. The applicability of computed tomography techniques to TEDDI data has yet to be investigated.

The time requirement for each data set collection is determined largely by the thickness and absorbance of the sample object (assuming that all or most of the sample components are crystalline). It varies quite widely. In favourable cases 30 seconds per data set may be sufficient, whereas for, say, a concrete block 5 cm in thickness 3–5 minutes may be required. It is especially important that we allow adequate time for each data acquisition if we are looking to locate minority components in the sample, since otherwise the main features of interest in the data may be too indistinct to be of real use. The subject of count statistics and data quality needs to be addressed here, particularly as it tends to be neglected in the synchrotron EDD literature dealing with less severe applications, where satisfactory count statistics can safely be taken for granted.

1.3 Data Quality
By 'data quality' we primarily mean the peak-to-noise ratio as observed in the diffraction pattern (as opposed to the detector signal-to-noise ratio, which affects peak widths). Noise is an intrinsic feature of all diffraction patterns. Strictly speaking we can never eradicate it, but by acquiring data for long enough we can aim to average out the noise over the data acquisition period. The problem here is that this effect may be difficult to attain with the weakest peaks in the pattern, which can be a serious limitation on the detection of minority phases in the sample. Despite the great intensity and penetration of the synchrotron beam, we need to remember that TEDDI is a particularly demanding application, and maintain a certain realism about statistical limitations.

Figure 4 is intended to illustrate the problems that may arise when the presence of noise is combined with peak overlap. In plots (a) to (c), the solid lines show the results of adding simulated 'Poisson noise' to the sum of two calculated, overlapping Gaussian peaks; in Figure 4(d) no noise has been added, in order to show the ideal combined profile. The noise has been generated to simulate the condition that each observed datum y_n(obs.) composed from
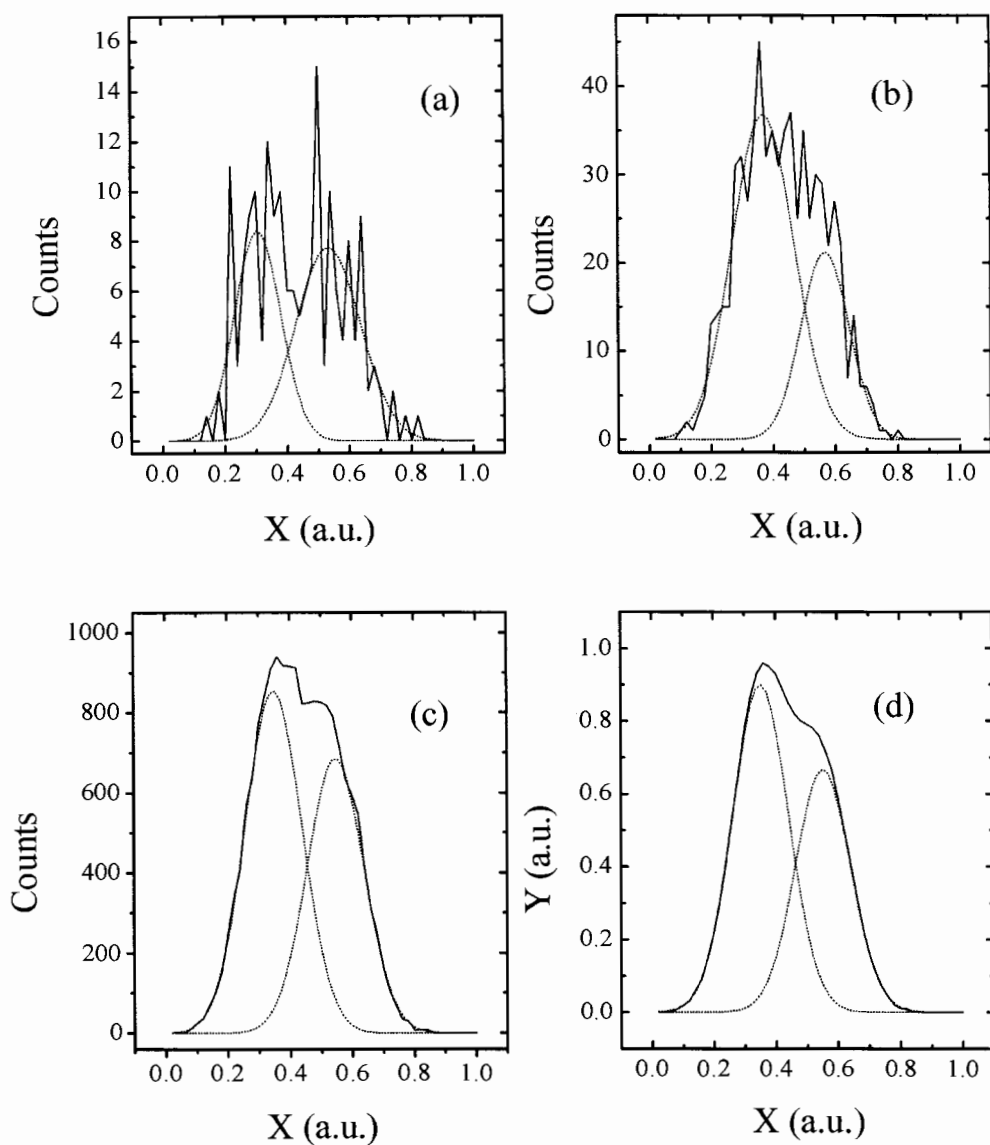
Figure 4. Simulated Poisson noise added (plots (a), (b) and (c)) to calculated gaussian peaks shown in (d). The signal-to-noise ratio depends on the intensities of the peaks, as indicated by the different vertical scales. Dotted lines show the 2-gaussian least-squares fit results for each case.

y_n(ideal)+y_n(noise) is an estimate of y(ideal) with an estimated standard deviation (esd) of $\sqrt{y}$(ideal). Plots (a), (b) and (c) in Figure 4 show the typical effects of Poisson noise on progressively more intense peaks. Taking the relative esd $\sqrt{y}/y = 1/\sqrt{y}$ as a reasonable measure of peak-to-noise ratio, we would expect the noise to be less and less significant as peak

intensities increase, and the plots show clearly that this is indeed so. Unfortunately, we must also expect to spend n^2 times as long acquiring data to obtain a general n-fold improvement in peak-to-noise ratio. We would have to increase data collection time by a factor of 100 to see a profile as well defined as in Figure 4(c) in place of that in Figure 4(a). On the other hand, by quadrupling the nominal intensity time we have already the noticeable improvement seen in Figure 4(b). There is a law of diminishing returns regarding data quality with respect to collection time, as with many other experimental methods.

The noise problem becomes still more evident when we apply least squares fitting to the noisy data, to obtain a measure of the apparent peak intensities and positions. Our aim is to recover the two noiseless Gaussian distributions from the data. The actual results of this procedure are plotted as dotted curves in Figure 4. Ideally, the fitted peaks should be centred on 0.35 and 0.55 respectively on the arbitrary x axis, with equal widths of 0.2 and an intensity ratio of 4:3, as shown in Figure 4(d). Not surprisingly, the procedure is not particularly successful in case (a), where the noise has misled the least-squares algorithm into assigning too much width to the second peak. The intensity ratio obtained here is about 3:4, far from the original value, and furthermore, position errors are about 25% of the full-widths-at half maxima (FWHM), which is too inaccurate for reliable phase identification to be made. In case (b) the situation is significantly better, in that the first peak is now measured as more intense than the second, and positions are determined to within 5% of the FWHM. Here again, though, peak width estimation is rather poor, giving an exaggerated intensity ratio of 9:4. In case (c), excellent agreement with expected values is obtained from the fitting process. In designing a TEDDI experiment, we aim to have at least the stronger peaks as well defined as in Figure 4(c), if not better. Weaker peaks as in 4(b) may give useful phase identification provided we have some prior knowledge of possible components in the sample. Very weak peaks such as shown in 4(a) can be given only speculative interpretations at best, unless they can be linked to other stronger peaks in the same pattern. As so many parameters are involved in any given experimental case, it is difficult to derive a lower limit of detection in terms of phase concentration within the diffraction needle, from a limit in terms of diffraction peak height. Experience suggests, however, that about 1% by weight is a reasonable estimate of attainable sensitivity. The relationship between statistical data quality and accuracy of d-spacing measurement is at least as important as that between d-spacing measurement and peak width, a fact not always made clear in the literature. In practice, we can sometimes obtain more reliable position and width information on the weaker peaks by summing a number of spectra in which they occur, and using this information when treating the individual data sets. Even then, the resulting intensity data may be of little use if the phase is widely diffused through the sample. For very demanding applications some trial and error may be necessary to find the best experimental parameters, but of course this is likely to entail a considerable expense of synchrotron beamtime.

The typical EDD peak FWHM is about 0.3 keV, though this can be greater if the crystallites are very small [4]. Thus the Bragg equation (2) can be used to predict the degree of overlap which may be expected between the peaks from a given mixture of phases. (For instance, there are some unfortunate overlaps between the peaks from two of the commonest minerals, quartz and calcite, though this is usually not disastrous if we choose the well-resolved peaks for analysis.)

Ideally the relative intensities of the peaks due to any given sample phase should reasonably resemble those tabulated in the ICDD database. To understand why we cannot place too much reliance on this, we need to consider in more detail the effect of sample characteristics on the data we obtain.

2. MATERIALS CONSIDERATIONS

The TEDDI experimental set-up is quite different to that of ASD. Whereas the latter looks at relatively small volumes of samples sitting on a variety of sample stages the TEDDI experiment non-destructively collects diffraction information from real, intact objects. Of course there has to be a limit on the size of object we can investigate and the size of the image we can collect. These limiting factors are tied in with the sample composition, phase distribution, crystalline character, synchrotron radiation characteristics and the time restraints on synchrotron experiments. The sample and materials concerns that we address in the following section should help in deciding if TEDDI is the best technique to apply to a given problem or in designing a TEDDI experiment. The discussion is based on both theoretical and empirical studies.

2.1 Texture and Sampling

To obtain a usable powder diffraction pattern, one that allows phase identification and quantification, there must be a large number of randomly oriented crystallites in the diffraction volume. This gives an unbiased 'powder average' in which all orientations are equally represented. As with ASD, the occurrence of texture in the samples and its effect on the diffraction data is a concern in the interpretation of TEDDI data. In TEDDI, however, we are looking at intact objects, and there is no opportunity to reduce the grain sizes by grinding, or to improve poor sample packing. Also, spinning the sample to improve particle statistics is only rarely an option in the sort of experiments we are concerned with here. To exacerbate the problem, a wide range of grain sizes and large inclusions often occur in the metal or rock objects that are being investigated. As the grain size of the powder increases so the numbers of crystallites decreases until there are too few of them for the powder averaging condition to be properly realised. Diffraction patterns from samples like this suffer from poor particle statistics and often no longer provide the material's characteristic 'signature'. (A crystallite is the same as a grain only if the grain in question is a small single crystal; since this is not always the case, the term 'grain' is used for the sake of generality).

The TEDDI probe is a long thin needle-like volume with linear dimensions in the range 0.1–0.5 mm in the plane normal to the incident beam, and several mm in length along the direction of the beam. This makes calculating the number of crystallites available for diffraction somewhat difficult. Given its needle-like shape, the diffracting volume in a 'real' sample with a distribution of grain sizes could contain many more crystallites than a simple volumetric calculation would predict. This is because a significant proportion of the larger crystallites might be only partially contained in the needle.

Table 4
Diffracting needle volumes and crystallite numbers for a range of different grain sizes

Square beam size (mm^2)	Needle volume* (mm^3)	Number crystallites
0.01	0.028	224
0.04	0.115	920
0.25	0.716	5728

*assuming a solid specimen with no voids
[†]detector 2θ angle = 2°, linear dimension of grains=50 μm
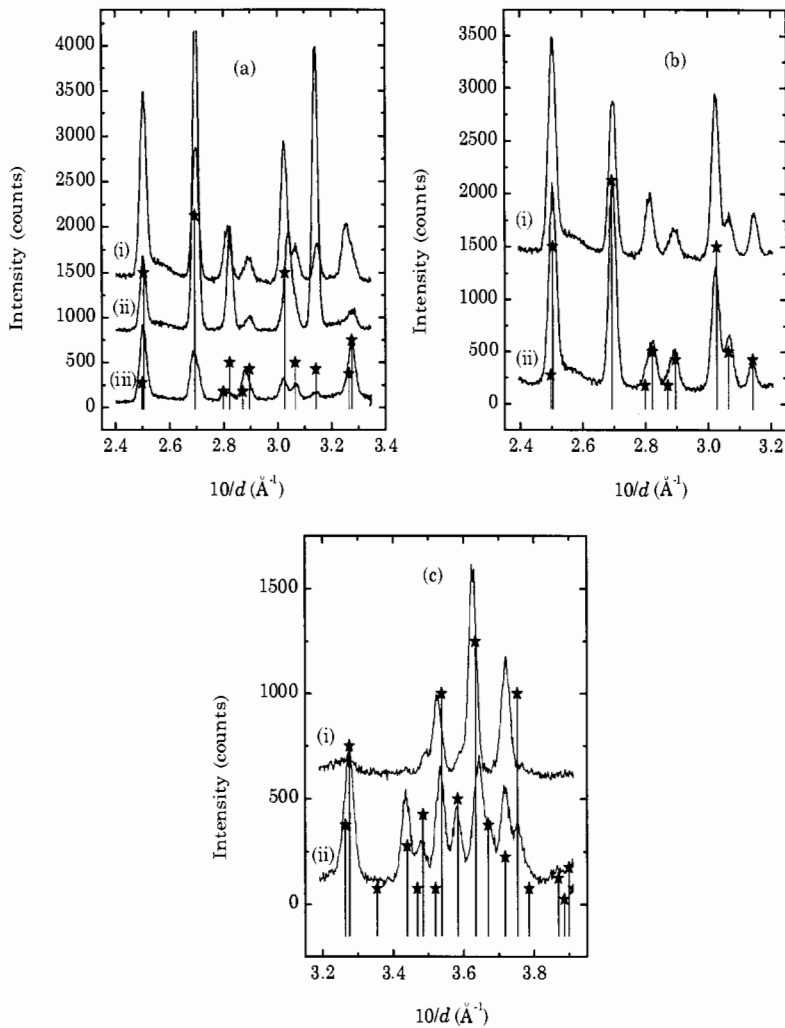
Figure 5. These diffraction spectra were collected from $CuSO_4.H_2O$ ground and sieved to a range of grain size distributions. (a) (i) has grains size x. $x < 38$ μm; (ii) 75 μm< x <100 μm; (iii) 180 μm< x< 600 μm. (b) Grain size less than 38 μm (i) stationary; (ii) spinning (60rpm). (c) Grain size 180 μm< x< 600 μm (i) stationary, (ii) spinning (60rpm). The stick plots are the ICDD peak positions for $CuSO_4.H_2O$ the lines have been scaled to reflect the intensity ratios in the diffraction file. The plots have been offset for clarity and only a section of the complete spectra are shown.

Table 4 gives theoretical values for the volume of the diffracting needle and the minimal estimate of the number of crystallites intersecting this volume.

Figure 5 illustrates the effect of texture with real data collected on Station 16.4 at SRS Daresbury. In this experiment diffraction spectra were collected from $CuSO_4.5H_2O$ powders that were ground and sieved to a range of crystallite sizes. EDD spectra were then collected over 180 seconds for each grain size. In Figure 5(a) we see how the intensity of the spectrum increases as the grain size decreases, since then the number of diffracting crystallites increases. For the smallest grain size used (<38 μm) all the expected reflections are present, and their relative intensities match closely those tabulated in the ICDD database. From such data, phase identification would be straightforward. With larger grains (between 180 and 600 μm) the relative intensities are skewed. From data such as shown in Figure 5(a)(iii) phase identification would be fairly easy given some prior knowledge of the sample, but less assured otherwise.

The datasets in Figure 5(a) were obtained with a spinning sample. In the majority of the kinetic experiments using EDD the sample cells are spun to improve the particle statistics. In TEDDI experiments such spinning around any axis perpendicular to the beam direction would have a very deleterious effect on the spatial resolution, but these are the only axes along which it is relatively easy to introduce spinning. The ideal axis for spinning, which would not introduce any loss of spatial resolution, is along the direction of the beam, but this would be mechanically very difficult to achieve such a motion with the necessary precision. Figure 5(b) shows that for small grain sizes (less than 38μm) there is no significant advantage to be gained by spinning the sample. However, Figure 5(c) shows that where the sample is stationary, larger grain sizes (between 180μm and 600μm) lead to poor particle statistics, resulting in loss in intensity, absent reflections and anomalous relative intensities. The effect of oscillating the sample about a vertical axis passing through the centre of the diffracting needle has been investigated. This motion improves the particle statistics by 'sweeping' more crystallites into the diffracting volume, but it also changes the volume sampled to a bow-tie shape. Although this is preferable to full rotation, it still significantly degrades spatial resolution. For example, a 2° oscillation would smear a 100 μm wide beam to 250 μm.

Investigating materials with large inclusions and/or large grain sizes will be problematic for *ab-initio* phase identification. One aid in this process is to use the spatial correlations that become apparent in scanned datasets. From correlated changes to groups of reflections it is possible to associate them and perform database searches. Search and match software routines specifically for EDD data have not been devised, as far as the authors are aware.

2.2 Composition and X-ray Absorption

In transmission geometry the absorption of both incident and diffracted beams determines the size limits of objects that can be investigated and the length of time for data collection. The more absorbing the material (*i.e.*, the higher the density and average atomic weight) the longer the count times required to collect enough diffracted photons to produce a good quality pattern. We can obtain data from very thick samples because the synchrotron provides a high flux of hard x-rays. The flux distribution with respect to photon energy at any white beam station is determined by the current and electron energy in the synchrotron storage ring, and the insertion devices used to boost/generate more flux.
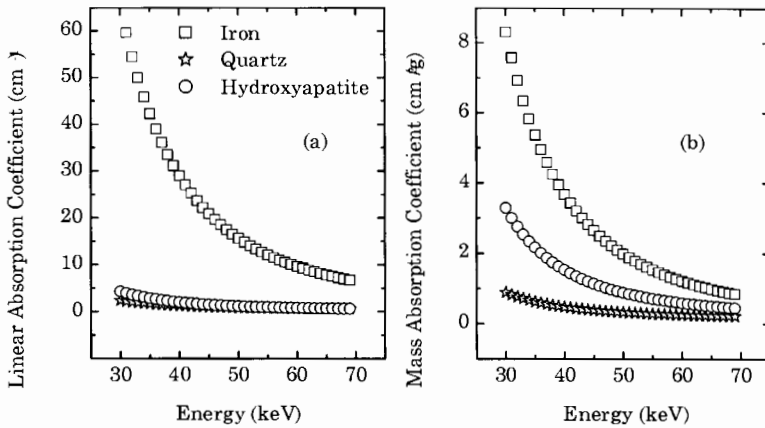
Figure 6. Linear absorption (a) and mass absorption (b) coefficients respectively over the 30-70keV x-ray photon energy range for materials: iron, quartz and hydroxyapatite.

We can estimate the thickness of material that a synchrotron x-ray beam can penetrate using standard tables and known densities to calculate the linear absorption coefficients [5]. For materials of interest such as iron, quartz and hydroxyapatite we can calculate the mass absorption coefficient as a function of photon energy using an empirical equation with parameters tabulated in the International Tables for X-ray Crystallography. The linear absorption coefficient μ is the product of the mass absorption coefficient and the sample density. The effect of beam absorption can be quantified as

$$I=I_0\exp(-\mu t) \tag{5}$$

where I is the resultant beam intensity, I_0 the incident beam intensity and t the thickness of material. For a given x-ray wavelength (*i.e.* energy) the total linear absorption coefficient (μ cm^{-1}) is characteristic of the absorbing material. In Figure 6 the linear and mass absorption coefficients for iron, quartz, and hydroxyapatite have been plotted for the x-ray energy range 30-70 keV. This energy range is typically the region with the highest flux for a synchrotron white beam station (see Figure 3). The softer x-rays (lower energy) are much more strongly absorbed than the harder x-rays and the metal is more highly absorbing than the minerals. Hydroxyapatite has a higher mass absorption coefficient than quartz. It is informative to plot the photon transmittance of these materials (I/I_0), as in Figure 7. At the hard x-ray end of the spectrum the beam will have 50% penetration through 12 mm of mineral material but only 3 mm of metal. At the soft x-ray end of the spectrum the x-ray beam is almost completely absorbed by 1 mm of iron, and by 10 and 16 mm of hydroxyapatite and quartz respectively.
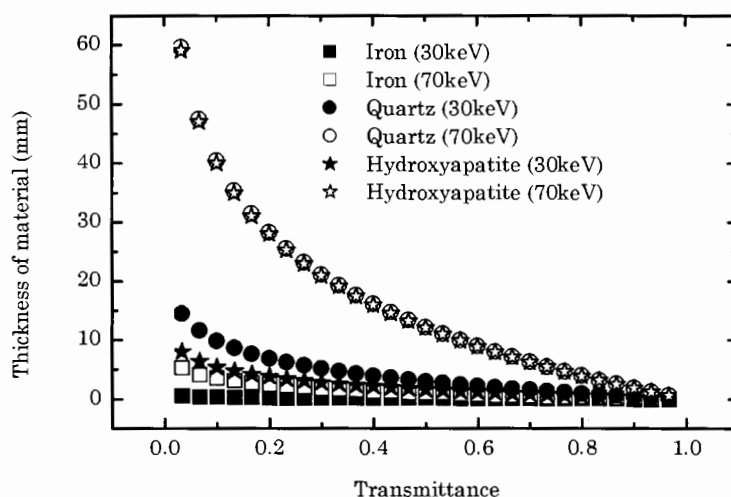
Figure 7. Calculated transmittance for photons with energy range 30-70 keV through iron (density 7.87 g/cm^3), quartz (density 2.65 g/cm^3) and hydroxyapatite (density 1.3 g/cm^3).

The general effect of absorption on a pattern is to impose an overall intensity envelope onto the diffraction spectra, in addition to that already imposed by the incident beam energy spectrum. In the case of a highly absorbing and/or thick object this would mean lower intensities in the 'softer' low energy x-ray region. A study of a bronze agricultural tool (C11th) illustrates the severity of absorption for metallic objects. The work was done on Station 9.7 at SRS Daresbury. Figure 8(a) shows a photograph of the bronze tool which is approximately 200mm in length and, whilst hollow, is 30mm in thickness. The enlargement of the tip of the tool in Figure 8(b) shows the x-ray sensitive paper over the region investigated. The scan was obtained by scanning the tool perpendicular to the beam in 21 incremental steps of 1mm and in a mutually perpendicular direction in 10 steps at 0.5 mm intervals. The individual dot marks along the 0.5mm scan cannot be resolved but most of the 21 lines indicating where the beam entered the sample are clearly visible. Each dataset was collected over 60 seconds. The diffraction pattern in Figure 8(c) shows the peaks that have been identified in a single dataset that is the summation of all the datasets along a single line as in Figure 8(b). Figure 8(d) is a 2D contour map illustrating the change to the spectra as the tool is moved transverse to the beam direction. At point 0 mm in the traverse the beam is not intersecting the tool. There is slight background intensity in the lower energy region, which is due to air scatter and secondary scatter from the edge of the tool. As the tool moves to intersect the beam the strongest peaks in the pattern at this point are the Sn $K\alpha_1$ and $K\beta_1$ fluorescence lines at 25.272 and 28.491 keV respectively and Cu $K\alpha_1$ and $K\beta_1$ lines at 8.048 and 8.905 keV. (The detected x-ray fluorescence originates from, not only the diffracting volume but also from along the diffracted beam path.) Where the beam intersects the tip of the tool the first diffraction peaks appear. These are three reflections from malachite at 5.93Å (I_{84}), 5.01Å (I_{96}), and 3.67Å (I_{100}), (subscripts refer to the intenities tabulated in the ICDD database, normalised to 100) and these, along with the fluorescence peaks grow in intensity as the traverse continues into the tool.
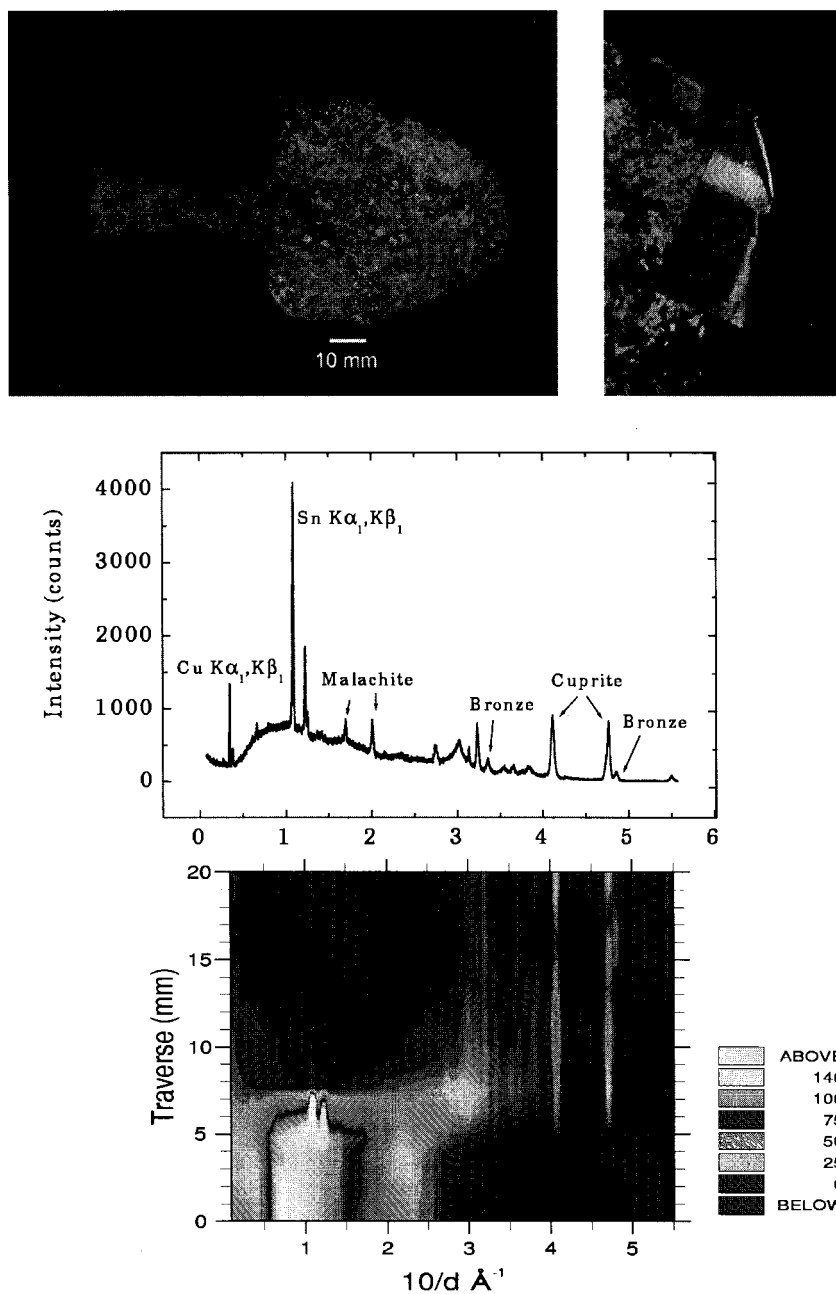
Figure 8. The photograph of the bronze tool in (a) has been enlarged in (b), where it shows the x-ray sensitive paper which marks the beam entry points on the tip of the tool. The plot in (c) shows the sum of 20 datasets taken along a 1D traverse of 20 mm. The 2D contour map (d) shows this data spatially resolved.

The edge of the tool has a wedge shape and as the thickness of material increases so there is a gradual loss in the signal in the soft x-ray region as these x-rays are absorbed. Once the thickest region of the tool (30mm) is in the diffracting volume (the diffracting needle is nominally 23mm in length and hence completely contained within the tool) so only x-rays in the high-energy x-ray region can penetrate the bronze tool. The high-energy region of the diffraction pattern has reflections from cuprite and bronze phases. By examining both the individual spectra and the correlations between spectra at different points on the traverse, it is fairly straightforward to identify and differentiate between surface phases, bulk phases. With more complex multi-phase materials, such as ceramics, phase identification and mapping requires prior knowledge of the material and accurate d-spacing values, as well as spatial information.

As absorption has a marked effect in determining the pattern profile so this physical effect can mask the contributions to the patterns from the materials chemistry. It is important to bear this in mind during the analysis. Also peak identification in diffraction patterns of alloys and minerals is also complicated by the possibility that peak positions have shifted due to variations in crystallographic unit cell dimensions caused by solid solution effects. In some instances the phase identification may need to be supported with higher resolution ASD or microscopy.

An experiment looking at the growth of minor mineral phases around rock aggregates in a concrete block illustrates the penetrating power of the beam on Station 16.4, SRS Daresbury. The block was rectangular (77x78x42 mm) with limestone and dolomitic aggregates in a cement/quartz matrix. The density of concrete is similar to that of quartz although it is a stronger x-ray absorber because of the quantities of higher atomic weight elements in the composition, especially calcium, and iron.

The aggregate pieces ranged in size from sub-millimetre dimensions to over 15mm. The concrete block was positioned to overlap with the entire diffraction needle (13mm in length) and to contain, as far as could be guessed, a mix of aggregate and matrix phases. The rectangular block was placed in 3 orientations and a diffraction spectrum collected in each one. Details are given in Table 5. The quality of the patterns can be seen in Figure 9(a), obtained through the thinnest section of the block (37.5mm) has the greatest number of peaks with contributions from the aggregate and the matrix. A minor cement hydrate phase, ettringite (less than 1% by weight) is also detected.

Through the thickest dimension (77.5mm), Figure 9(c), we see that the number of strong peaks has greatly decreased. As the strongest two peaks are from the same phase and this is an aggregate phase, we may deduce that the needle was positioned almost entirely within a single piece of aggregate. This could be confirmed with a 2D/3D traversed data collection, which would produce a map of the area around this point. An example of this type of map is given later.

Table 5
Diffraction spectra obtained through a concrete block, Figure 14

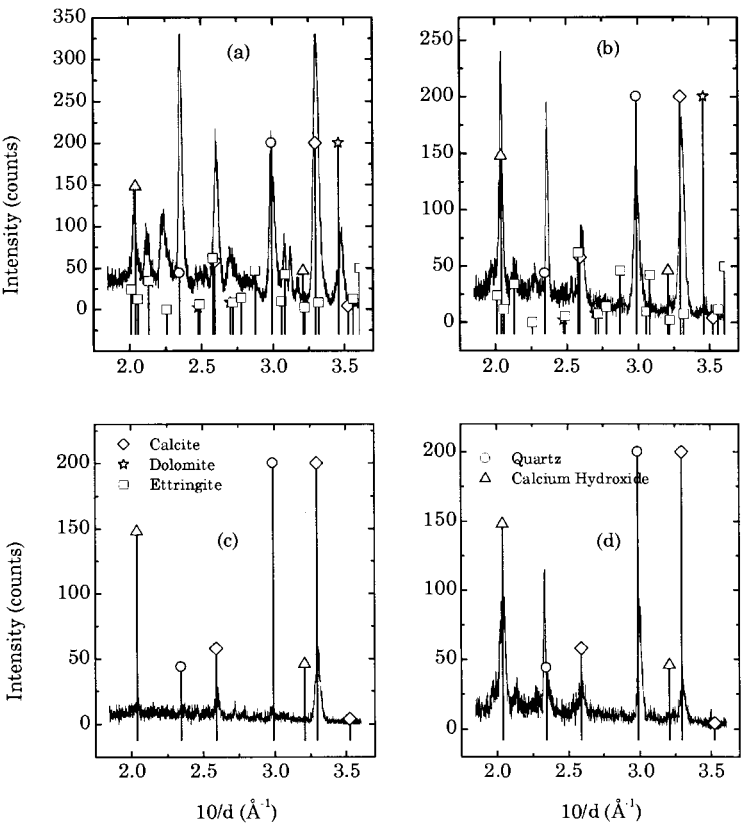| Plots	Thickness of concrete (mm)	Data collection time (seconds)	Height of calcite I_{100} reflection (counts)
(a)	37.55	300	328
(b)	47.55	300	168
(c)	77.46	300	54
(d)	47.56	120	28

Figure 9. Diffraction patterns collected through various thickness of concrete. See Table 5 for details.

Comparison of Figure 9(b) and (d) clearly shows the advantage of longer count times. Figure 9(b), which was collected in over twice the time of Figure 9(d) has a better peak to noise ratio and overall intensity.

2.3 Resolution

Without the use of computed tomography techniques and reconstruction algorithms, the spatial resolution of the TEDDI technique is compromised by the high aspect ratio of the diffracting volume. The smallest dimensions of the needle are determined by the beam slits pre- or post-sample and these dimensions can be as small as 10 microns. Using the smallest beam dimensions then has the associated problem of low photon count rates. The limits on the step size for translating the object are determined by the engineering restraints on the stage. In the simplest linear traverses of the stage it is driven either in mutually perpendicular directions to the beam direction or along the beam direction. In the latter cases the step dimensions can be set to be similar to the slitted-beam width. Where the step size is the same as the needle width then the limit of resolution is the needle width. Where the step size is smaller than the beam width then the limiting factor of resolution is the step size and the

image obtained is a convolution of the signal from the object and the needle width. An example of a 2D traverse perpendicular to the beam is given in Figure 10. The sample shape, in this case, lent itself favourably to the needle shape of the diffracting volume. It is a cement micro-engineering structure with 120x120 µm high and wide channels that were of the order of a few millimetres in length. The sample was aligned face-on to the incident beam and moved in 25 µm steps along the width of the channels (range 2.5mm) and 100 µm steps along the height of the channels (range 0.4mm). The beam width was set at 100 µm. The point of interest in this study was the distribution of a particular mineral addition, mordenite, to the cement, between the base and the channel features. The analysis of the complete diffraction spectra, of which there were 200, involved extracting the diffraction information on the mordenite, calcium hydroxide (a cement hydrate) and tricalcium silicate (a cement-starting phase). The 2D diffraction contour maps in Figure 10 reveal the crystalline content of the channels and provide semi-quantitative information on the distribution of these phases between the channel and the bulk of the material. In this case TEDDI has reproduced the shape of the object, and provided information on its microcrystalline content with a spatial resolution better than 100µm.
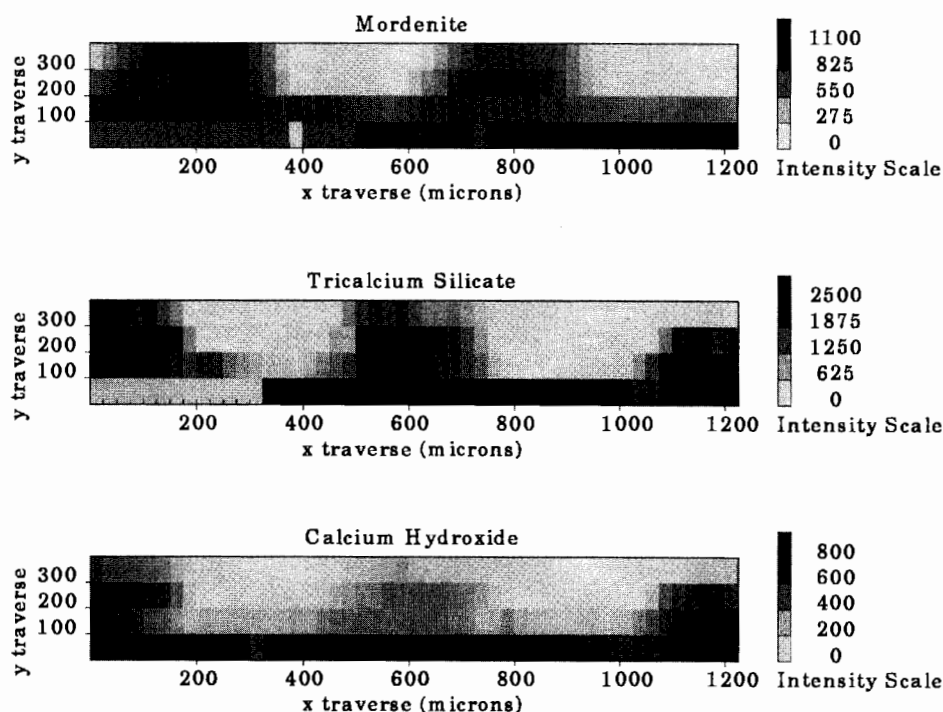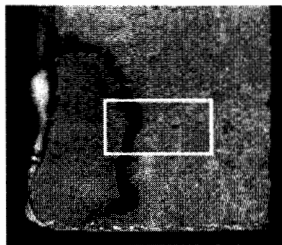

Figure 10. 2D phase maps of a cement micro-engineering structure showing the distribution of the crystalline phases; calcium hydroxide, tricalcium silicate and mordenite through the 100 µm wide channels. The area of low intensity marks the void space between the channels.
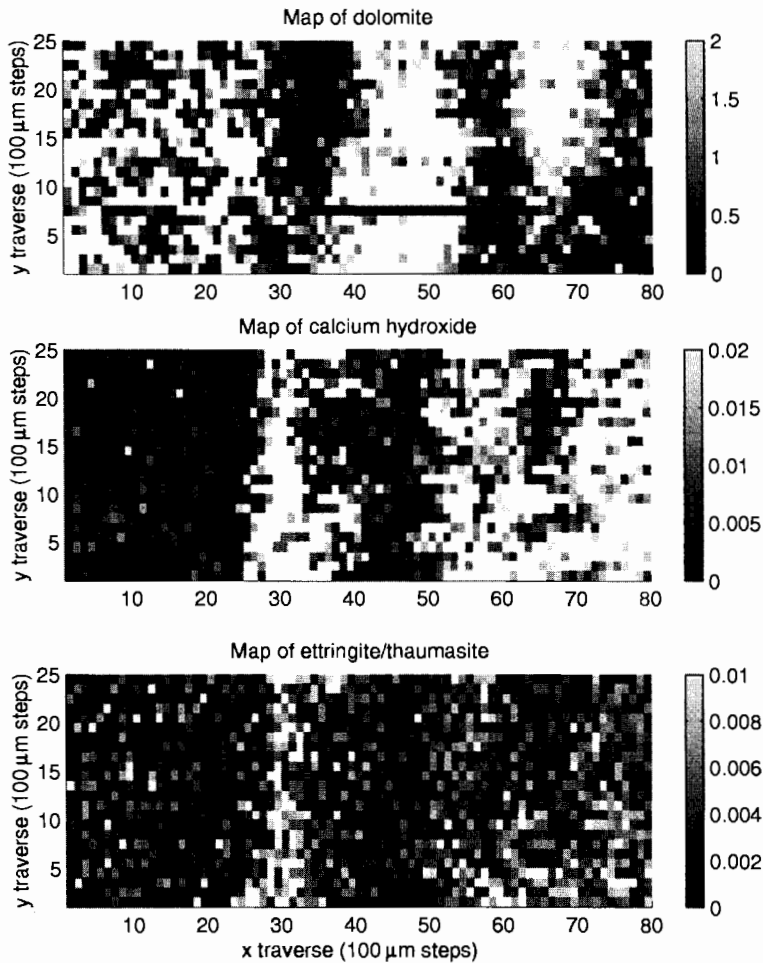
Concrete rock sample (8×2.5 mm box inset.)

Figure 11. The photograph at the top of the page is of the concrete block. The depth of the block along the beam path was 4 cm and diffraction volume was several millimeters inside the block. The 2D phase maps above show the distribution of the cement phases around the aggregate (dolomite).

A similar TEDDI investigation was made of the interior of a larger object, a concrete block. In this case the feature of interest is the aggregate/cement interface and the occurrence of particular phases at this interface. Figure 11 shows the concrete block and similar 2D contour maps for this work. In this experiment the diffracting volume was completely inside the concrete block but the volume under investigation was selected with reference to large aggregates on the surface. In interpreting these data it is important to remember that the 2D pixellated representation is the projection of the phase information along the length of the diffracting needle (approximately 3.8 mm). This could explain the left-hand region of the map where there is a strong but not continuous signal from the aggregate and a dispersed signal from the cement phases. Here the diffracting volume may, along its length, have intersected with both cement and aggregate phases. A 3D scan, *i.e.,* a depth traverse along the length of the beam, would have fixed the position and size of this piece of aggregate. Yet despite this resolution handicap we are still getting spatial resolution on a 100 μm scale. We cannot expect to distinguish spatially between the microcrystalline phases of calcium hydroxide and ettringite, but we can see the distribution of these phases around the larger aggregate. What is really exciting about these images is that they were collected from the interior of a 4 cm block of concrete!

These two examples of work done on industrial materials have demonstrated a spatial resolution down to the order of 100 μm for the technique. An early piece of work at the European Synchrotron Radiation Facility (ESRF) on test objects [6] has shown that with a small beam size, small step size and suitably sized sample, spatial resolution down to the order of a few microns is possible.

There have been other applications of TEDDI to archaeological objects which highlight all the good points that we have already discussed; investigation of weathering on a temple frieze from Ankor Wat, Cambodia [7], a Grecian ceramic pot sherd [8]. Each of these studies has non-destructively revealed the interior crystalline character of these objects. These experiments discussed above were both performed on 'real' samples, *i.e.* solid 'as-found' objects rather than powders or prepared surfaces.

In conclusion we can say that TEDDI has unique capabilities for the characterisation of solid objects.
1. It is non-destructive.
2. It reveals details of the internal phase composition of even relatively bulky sample objects.
3. It has potential for high spatial resolution.
As has been pointed out, the technique has certain specific limitations, but it is hoped that there will be many applications for which TEDDI will be a new and exciting tool.

REFERENCES
1. B.C. Giessen and G.E. Gordon, Science, 159 (1968) 73.
2. Buras and L. Gerward, Prog. Cryst. Growth Char., 18 (1989) 93.
3. S.D.M. Jacques, PhD thesis, London University (1999).
4. L. Gerward, S. Mørup and H. Topsøe, J. App. Phys. 11 (1976) 137.
5. D.C. Creagh and J.H. Hubbell. *X-ray absorption (or attenuation coefficients).* In International Tables for Crystallography Volume C (Ed. A.J.C. Wilson. Kluwer: Dordrecht). Chapter 4.2.4. (1992) pp189-206.
6. C. Hall, P. Barnes, J. K. Cockcroft, S. L. Colston, D. Hausermann, S. D. M. Jacques, A. C. Jupe, M. Kunz, Nucl. Inst. Meth. Phys. Res. B 140, (1998) 253-257

7. P. Barnes, S. Colston, A.C. Jupe, S Jacques, J. Cockcroft, A. Bennet, C. Hall, Proc. Eur. Cryst. Com. Prague, (1998) in press.
8. E. Pantos, C.C. Tang, E.J. Maclean, K.C.Cheung, R.W. Strange, P.J. Rizkallah, M.Z. Papiz, S.L. Colston, B.M. Murphy, S.P. Collins, D.T. Clark, M.J. Tobin, M. Zhilin, K. Prag and A.J.N.W. Prag, Synchrotron Radiation in Archaeometry, Proc. EMAC99, 5th Eur. Meeting on Ancient Ceramics, Athens (1999).